Design Considerations to Reduce Gap Variation and Misalignment Effects for the Inductive Power Transfer System

Cong Zheng, *Student Member, IEEE*, Hongbo Ma, *Member, IEEE*, Jih-Sheng Lai, *Fellow, IEEE*, and Lanhua Zhang, *Student Member, IEEE*

***Abstract*—An inductive power transfer (IPT) system usually consists of four parts: an ac–dc power factor correction (PFC) converter, a high-frequency dc–ac inverter, a compensation network comprising a loosely coupled transformer (LCT) and the resonant capacitors, and a rectification output circuit. Due to the relatively large air gap, the magnetic coupling coefficient of the IPT system is significantly lower than that with tightly coupled transformer. As a result, the efficiency of the IPT system is always a main concern for applications with possible gap variation or misalignment condition. To ensure high power transfer efficiency, these IPT systems should have high tolerance for different gap variation and horizontal misalignment conditions. In this paper, the effect of coupling coefficient deviation to compensation network efficiency is analyzed, and design considerations to reduce gap and misalignment effects for the IPT system are proposed. By using finite-element analysis simulation method, the performance of different transmitter and receiver coil dimensions is compared. In order to validate the performance of the proposed design considerations, a 100-W hardware prototype with two sets of LCT is built and the corresponding experiments are carried out. As compared to the symmetrical LCT architecture, the proposed asymmetrical LCT prototype improves the coupling coefficient reduction from 68% to 28% when the gap varies from 6 to 20 mm and from 89% to 31% when the misalignment ranges from 0 to 50 mm. Therefore, the efficiency deviation for the asymmetrical LCT is maintained within 3.5% over the entire tested gap variation and misalignment ranges.**

***Index Terms*—Finite-element analysis, inductive power transfer (IPT), loosely coupled transformer (LCT), misalignment.**

I. INTRODUCTION

NOWADAYS, inductive power transfer (IPT) systems are gaining considerable attention due to the increasing dependence on various battery-powered applications, such as contactless battery charging for electric vehicles (EVs) [1]–[8], portable electronic devices [9]–[12], biomedical implants [13]–[20], and so on. Major drawbacks of traditional conductive power transfer systems are the wiring associated trip hazards and the contact wear-out. In an effort to overcome these drawbacks, an IPT system such as the one depicted in Fig. 1 demonstrates many advantages including convenience of being cordless making it unnecessary to plug and unplug the bulky cable, insusceptible to weather impact since the primary side can be embedded underground for EV charging applications, significant reduction to an implant system's footprint, and inherently safe during charging since there is no exposed conductors.

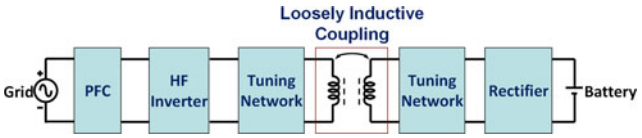

Fig. 1. Typical diagram of the IPT system.

Despite those advantages, there are still some issues to be addressed for IPT systems. As an example, gap and horizontal misalignments between transmitter and receiver would be a critical problem because the power transfer efficiency greatly depends on the relative positions of the primary and the secondary coils in the IPT system. Therefore, the power transfer efficiency is drastically reduced when a gap variation or misalignment occurs between the inductive coils [19], [20]. For EV charging applications, different vehicle ground clearance or misaligned parking of the vehicle will result in the IPT system operating at a degraded performance of lower power transfer, reduced efficiency, and longer charging time. For biomedical implants applications, the coils are usually misaligned, because doctor or patient could not easily identify the implant location or orientation in regular outpatient or home settings. Therefore, one may have trouble to precisely place the transmitter coil, which often is embedded in a belt or clothes, held by hands or supported with a bedside apparatus, in the correct or optimal position outside the body. Moreover, relative body motions in daily activities or organ/tissue movement also create uncertainty in estimating the implant position from outside the body. Therefore, the coupling coefficient is unavoidably impaired.

The effects caused by gap variation and horizontal misalignments between primary and secondary coils should be fully addressed in order to enhance the efficiency and stability of the IPT system. One possible solution is to employ additional coils either in the primary side or in the secondary side so that the effects of gap and misalignment are reduced over a

Manuscript received September 30, 2014; revised January 10, 2015 and March 8, 2015; accepted April 14, 2015. Date of publication April 21, 2015; date of current version July 10, 2015. This work was supported by Texas Instruments Incorporated. The original paper manuscript has been presented at the *40th Annual Conference of IEEE Industrial Electronics Society*, October 29–November 1, 2014, Dallas, TX, USA. This paper has been modified and more analysis and test results have been incorporated compared to the conference paper. Recommended for publication by Associate Editor G. A. Covic.

C. Zheng, J.-S. Lai, and L. Zhang are with the Future Energy Electronics Center, Virginia Polytechnic Institute and State University, Blacksburg, VA 24061 USA (e-mail: czheng@vt.edu; laijs@vt.edu; lhzhang@vt.edu).

H. Ma is with the School of Information Science and Technology, Southwest Jiaotong University, Chengdu 610031, China (e-mail: mahongbo81@gmail.com).

Color versions of one or more of the figures in this paper are available online at http://ieeexplore.ieee.org.

Digital Object Identifier 10.1109/TPEL.2015.2424893

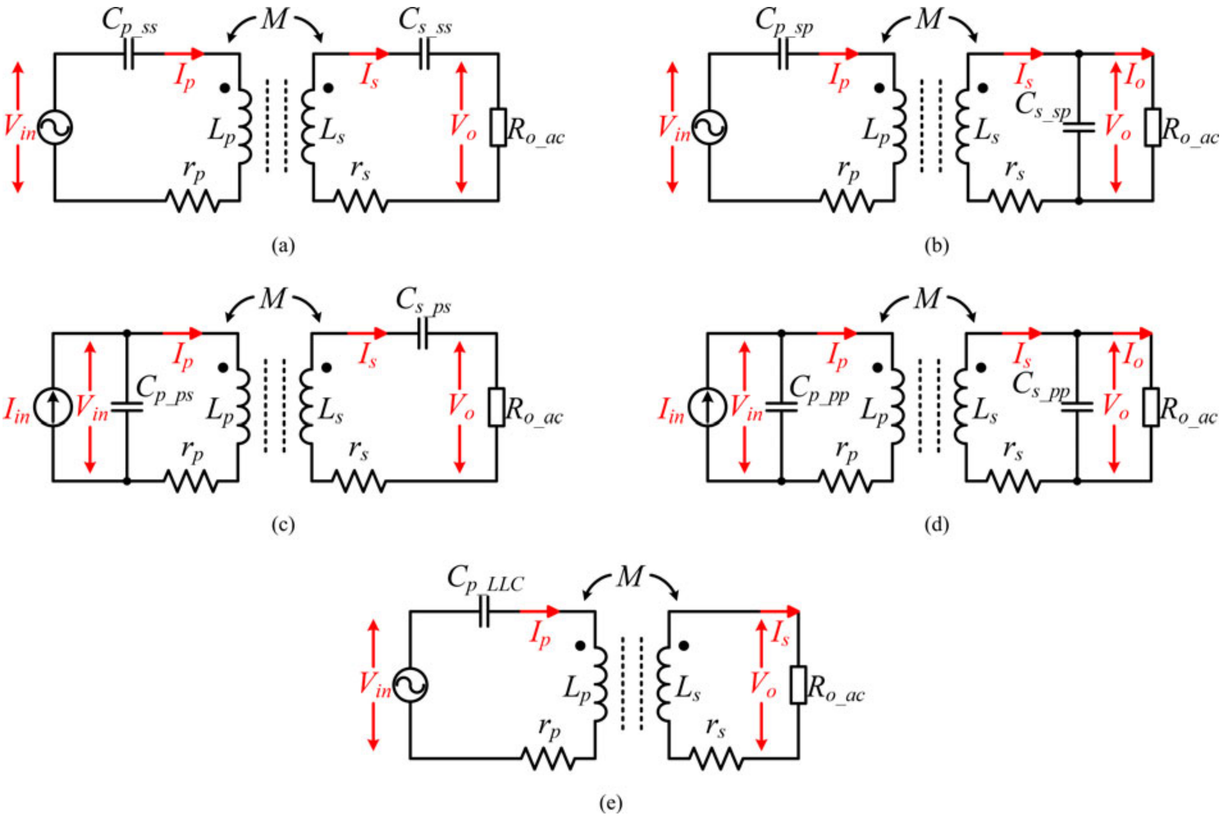

Fig. 2. Two-coil inductive coupling compensation networks of the IPT system: (a) SS, (b) SP, (c) PS, (d) PP, and (e) LLC.

TABLE I
PRIMARY AND SECONDARY IMPEDANCE

Circuit Type	Z_p	Z_s
SS	$r_p + j\omega L_p + 1/j\omega C_p$	$r_s + R_{o\_ac} + j\omega L_s + 1/j\omega C_s$
SP	$r_p + j\omega L_p + 1/j\omega C_p$	$r_s + j\omega L_s + \dfrac{1}{j\omega C_s + 1/R_{o\_ac}}$
PS	$r_p + j\omega L_p$	$r_s + R_{o\_ac} + j\omega L_s + 1/j\omega C_s$
PP	$r_p + j\omega L_p$	$r_s + j\omega L_s + \dfrac{1}{j\omega C_s + 1/R_{o\_ac}}$
LLC	$r_p + j\omega L_p + 1/j\omega C_p$	$r_s + R_{o\_ac} + j\omega L_s$

TABLE II
TOTAL IMPEDANCE OF FIVE CIRCUIT SYSTEMS

Circuit Type	**Total Impedance** Z_T
SS	$r_p + j\omega L_p + 1/j\omega C_p + \dfrac{\omega^2 M^2}{r_s + R_{o\_ac} + j\omega L_s + 1/j\omega C_s}$
SP	$(r_p + j\omega L_p + 1/j\omega C_p) + \dfrac{\omega^2 M^2}{r_s + j\omega L_s + \frac{R_{o\_ac}}{1 + j\omega C_s R_{o\_ac}}}$
PS	$\dfrac{1}{\frac{1}{(r_p + j\omega L_p) + \frac{\omega^2 M^2}{r_s + R_{o\_ac} + j\omega L_s + 1/j\omega C_s}} + j\omega C_p}$
PP	$\dfrac{1}{\frac{1}{(r_p + j\omega L_p) + \frac{\omega^2 M^2 (1 + j\omega C_s R_{o\_ac})}{R_{o\_ac} + (r_s + j\omega L_s)(1 + j\omega C_s R_{o\_ac})}} + j\omega C_p}$
LLC	$(r_p + j\omega L_p + 1/j\omega C_p) + \dfrac{\omega^2 M^2}{r_s + R_{o\_ac} + j\omega L_s}$

certain range [21]–[25]. One disadvantage of this solution is the required large surface area, since the available room is always limited, especially for receiver side. At the same time, the overall system cost and weight will be proportionally increased as the surface area enlarges. An alternative method that addresses these shortcomings is to retune the transmitter in order to operate at optimum switching conditions when the coils are in a misaligned state [26]–[32]. The main disadvantages of this solution are increased components count and more complex control strategy for the overall system. Some other researchers investigated the coil misalignment models as well as mutual inductance and coupling coefficient expressions based on mathematical derivations [33]–[37]. The shortcoming for these calculations is the loosely coupled transformers (LCTs) under investigation are always air-core coils. However, in practical implementation, in order to help shape the magnetic flux distribution and limit exposed radiative field to the ambient environment, some shielding techniques should be employed. Therefore, the derived mathematical expressions are no longer accurate under these realistic operation conditions.

It is known that coil dimensions and coil shapes substantially affect the magnitude of the magnetic field, which is closely related to the coupling coefficient of the LCT. In this paper, design considerations to reduce gap and misalignment effects for the IPT system are proposed. The paper is organized as follows. Section II introduces the circuit model of the IPT system including five compensation configurations, and the effect of coupling coefficient to the compensation network efficiency is carefully analyzed. In Section III, the relationship between the LCT coupling coefficient and several key parameters of the coil dimensions is analyzed using finite-element analysis (FEA) method. The analyzed results will allow the

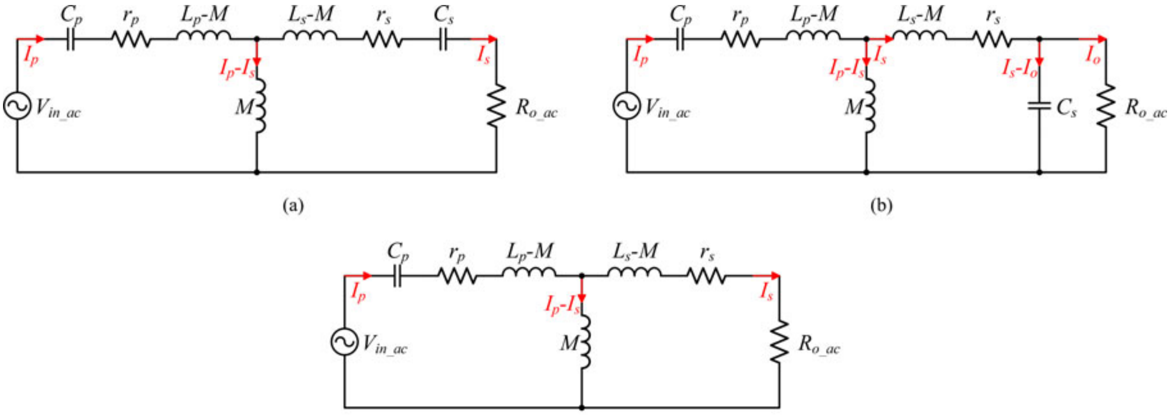

(a) (b) (c)

Fig. 3. Equivalent circuit with decoupled LCT model for (a) SS, (b) SP, and (c) LLC.

TABLE III
PARAMETERS VALUE OF COMPENSATION NETWORK

Parameters	Symbol	Value
Equivalent load resistance (Ω)	R_{o_ac}	4
Primary self-inductance (μH)	L_p	30
Secondary self-inductance (μH)	L_s	3.3
Mutual inductance (μH)	M	1, 2, 3
Primary capacitance (nF)	C_p	3.3
Secondary capacitance (nF)	C_s	30
Operating frequency (kHz)	f_s	200–800
Primary winding resistance (mΩ)	r_p	50
Secondary winding resistance (mΩ)	r_s	20

designer to optimize the efficiency of the inductive link and predict the effect of gap and misalignment on the coupling factor. Section IV describes that a 100-W lab prototype is implemented to validate the performance of the proposed design considerations, and the corresponding experiments are carried out. The experimental results reveal that the proposed asymmetrical LCT prototype greatly reduces the impact to the coupling coefficient as well as compensation network efficiency when gap variation or misalignment occurs. Finally, the conclusions are drawn in Section V.

II. CIRCUIT MODEL OF IPT

As illustrated in Fig. 1, an IPT system usually consists of four parts: an ac–dc power factor correction (PFC) converter, a high-frequency dc–ac inverter, a compensation network comprising a LCT and the resonant capacitors, and a rectification circuit connecting with the output load. There are various loads according to different applications. Loads used to recharging or heating can generally use equivalent impedance model composed of resistance and/or capacitance, hereinafter the resistive load is used to study the compensation circuit model and power transfer efficiency.

A. Equivalent Circuit Model

Five different kinds of two-coil inductive coupling circuit models are shown in Fig. 2, where Fig. 2(a)–(d) shows, respectively, the circuit model of series–series (SS), series–parallel (SP), parallel–series (PS), parallel–parallel (PP), and Fig. 2(e) shows the circuit model of LLC configuration. Coil resistances of primary side and secondary side are r_p and r_s, respectively. Coil self-inductances of transmitter and receiver are L_p and L_s, respectively. *M* represents the mutual inductance between transmitter and receiver coil. Resonant capacitances of primary and secondary tank are C_p and C_s, respectively. The subscripts _SS, _SP, _PS, _PP, _LLC indicate different compensation configurations. R_o_ac is the equivalent load resistance. Currents flowing

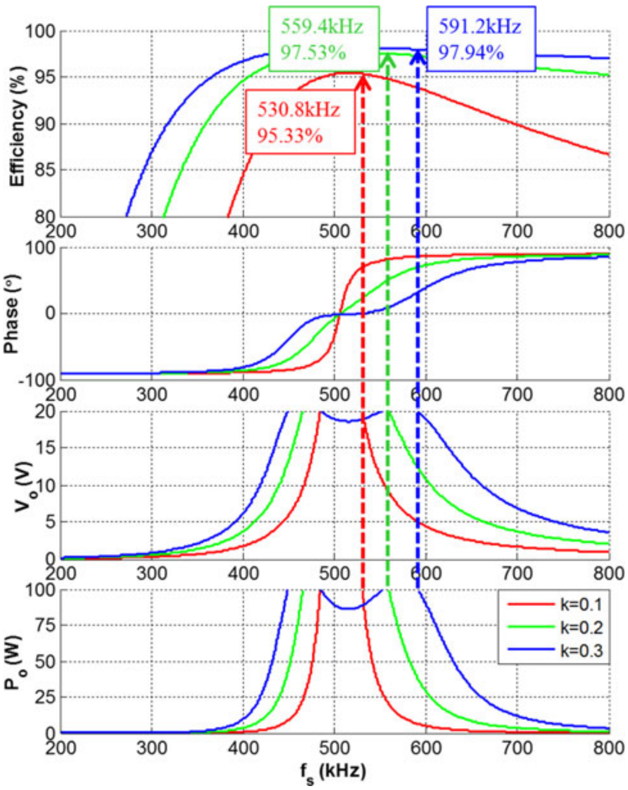

Fig. 4. SS compensation network efficiency, phase of total impedance, output voltage, and output power as a function of operating frequency for different coupling coefficients.

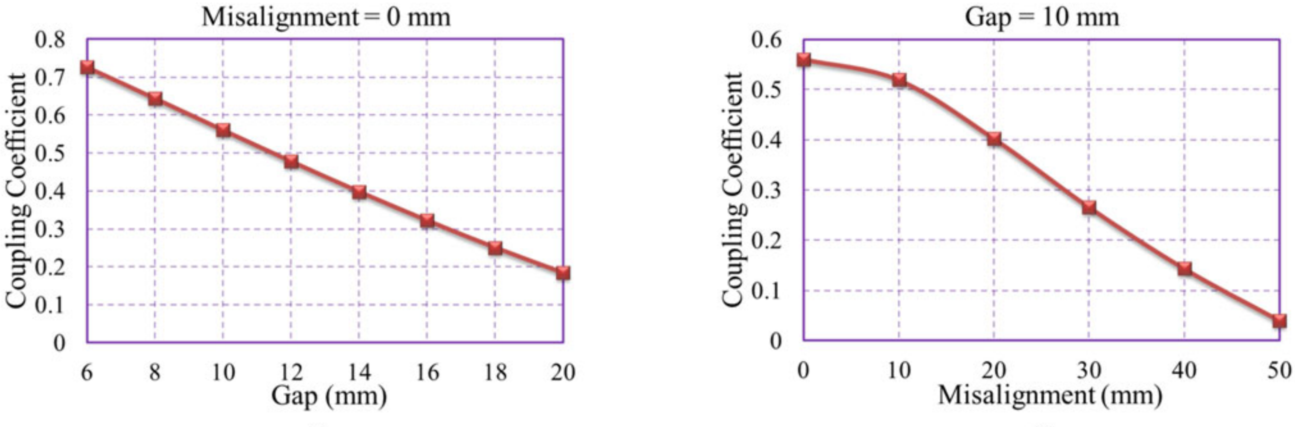

(a) (b)

Fig. 5. Coupling coefficient for symmetrical LCT as a function of (a) gap and (b) misalignment.

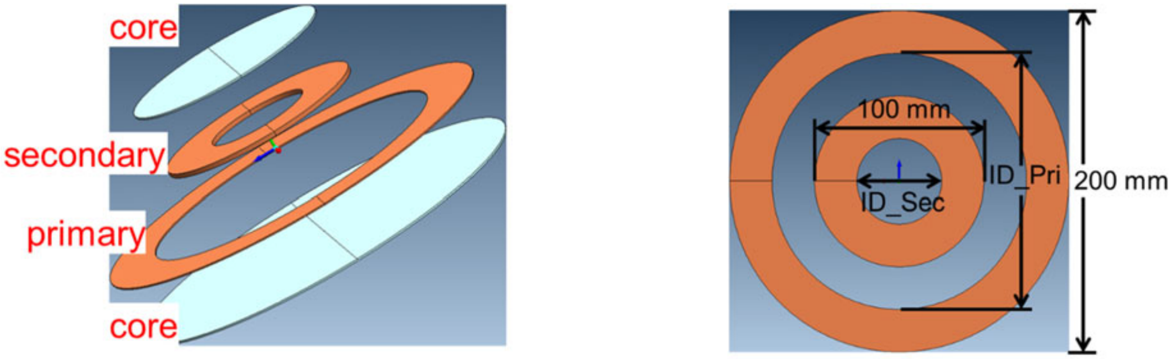

(a) (b)

Fig. 6. FEA simulation model. (a) Three-dimensional view. (b) Top view without ferrite cores.

TABLE IV
FEA SIMULATION PARAMETERS

Core Material	3C94
Plate Thickness	1 mm
Primary Core Diameter	200 mm
Secondary Core Diameter	100 mm
Primary Coil Thickness	0.74 mm
Secondary Coil Thickness	2.36 mm
Gap Distance	6–20 mm
Horizontal Misalignment	0–50 mm

through the transmitter coil and receiver coil are I_p and I_s, respectively.

Applying Kirchhoff's voltage law (KVL) to the above five coupling systems, their equivalent circuit in frequency domain satisfies the following equation:

$$\begin{bmatrix} V_{\text{in}} \\ 0 \end{bmatrix} = \begin{bmatrix} Z_p & -j\omega M \\ -j\omega M & Z_s \end{bmatrix} \begin{bmatrix} I_p \\ I_s \end{bmatrix} \tag{1}$$

where Z_p and Z_s are respective impedances of primary and secondary side, which can be expressed in Table I for the five different circuits.

From (1), we obtain

$$I_p = Z_p V_{\text{in}} / \Delta \tag{2}$$

$$I_s = j\omega M V_{\text{in}} / \Delta \tag{3}$$

where $\Delta = Z_p Z_s + \omega^2 M^2$.

The total impedance Z_T connected to the power source for five circuit systems can be expressed and shown in Table II.

B. *Efficiency of Compensation Network*

Fig. 2 shows that for a parallel resonant compensated primary (PS, PP), an equivalent current source is needed. Due to the difficulty of the energy storage in the form of a simple current source, extra components will be needed to transfer energy on demand from a voltage source, resulting in extra loss. Therefore, the following discussions in this paper are focused on the series resonant primary compensation configurations (SS, SP, LLC).

The IPT system dc–dc stage consists of three major components: high-frequency inverter, compensation network, and diode rectifier. The efficiency of the high-frequency inverter and diode rectifier are primarily dependent on the components selection when the power level is fixed. The efficiency of compensation network is affected by many factors, such as the

Fig. 7. Simulation circuit using (a) coupled inductor model and (b) decoupled model.

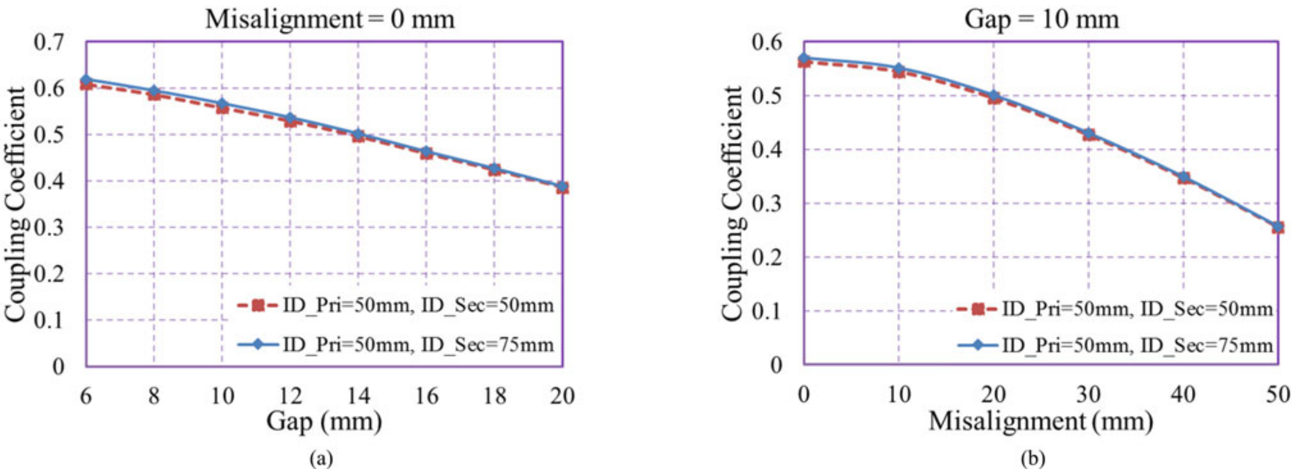

Fig. 8. Coupling coefficient when primary coil inner diameter is smaller than secondary coil outer diameter: (a) under gap variation but perfect aligned condition; (b) under misaligned but fixed gap condition.

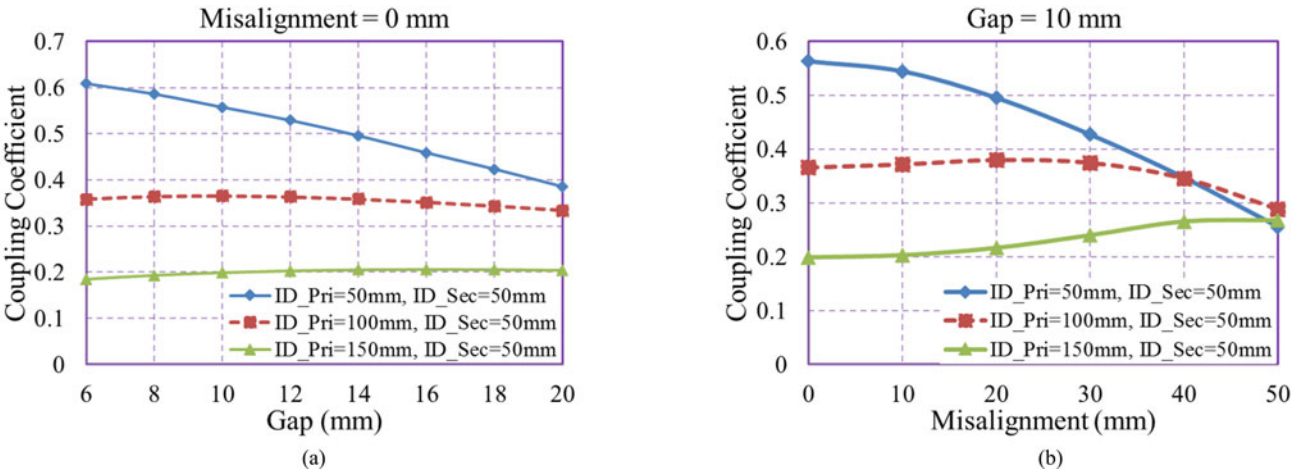

Fig. 9. Coupling coefficient for different primary coil inner diameter: (a) under gap variation but perfect aligned condition; (b) under misaligned but fixed gap condition.

LCT parameters, the compensation capacitances, the operating frequency, and the equivalent load resistance. Therefore, the design of compensation network is important to achieve high system efficiency.

To help analyze the efficiency of the compensation network, by adopting decoupled model for the LCT, the equivalent system models for SS, SP, and LLC compensation networks are depicted in Fig. 3.

Based on KVL, the relationship between primary coil current i_p and secondary coil current i_s for SS configuration is determined by

$$\begin{aligned}(I_{p\_\mathrm{SS}} - I_{s\_\mathrm{SS}})\, j\omega M &= I_{s\_\mathrm{SS}}\,(R_{o\_\mathrm{ac}} + r_s \\ &\quad + j\omega\,(L_s - M) + 1/j\omega C_s) \\ \Rightarrow I_{p\_\mathrm{SS}} j\omega M &= I_{s\_\mathrm{SS}}\,(R_{o\_\mathrm{ac}} + r_s \\ &\quad + j\omega L_s + 1/j\omega C_s)\,. \qquad (4)\end{aligned}$$

The output-to-input voltage gain can be expressed as follows: Eq. (5) as shown bottom of the page.

Combine (4) with the total impedance Z_{T_SS} in Table II, the high-frequency inverter supplied power $P_{\mathrm{in\_SS}}$, the power transferred to the equivalent load $P_{\mathrm{out\_SS}}$, and the efficiency of the SS compensation network η_{T_SS} can be derived as

$$P_{\mathrm{in\_SS}} = \left|I_{p\_\mathrm{SS}}\right|^2 \mathrm{Real}\left\{Z_{T\_\mathrm{SS}}\right\} \tag{6}$$

$$P_{\mathrm{out\_SS}} = \left|I_{s\_\mathrm{SS}}\right|^2 R_{o\_\mathrm{ac}} \tag{7}$$

$$\begin{aligned}\eta_{T\_\mathrm{SS}} &= \frac{P_{\mathrm{out\_SS}}}{P_{\mathrm{in\_SS}}}\\ &= \frac{R_{o\_\mathrm{ac}}}{R_{o\_\mathrm{ac}} + r_s + r_p \frac{(R_{o\_\mathrm{ac}}+r_s)^2 + (\omega L_s - 1/\omega C_s)^2}{\omega^2 M^2}}.\end{aligned} \tag{8}$$

Similarly, the efficiency and voltage gain of the SP and LLC compensation configuration can be calculated as Eq. (9) and (10) as shown bottom of the next page

$$\eta_{T\_\mathrm{LLC}} = \frac{R_{o\_\mathrm{ac}}}{R_{o\_\mathrm{ac}} + r_s + r_p \frac{(R_{o\_\mathrm{ac}}+r_s)^2 + \omega^2 L_s^2}{\omega^2 M^2}} \tag{11}$$

$$\begin{aligned}&\left|\frac{v_{o\_\mathrm{LLC}}}{v_{\mathrm{in\_LLC}}}\right|\\ &= \left|\frac{j\omega M \cdot R_{o\_\mathrm{ac}}}{\omega^2 M^2 + (r_p + j\omega L_p + 1/j\omega C_p)(r_s + R_{o\_\mathrm{ac}} + j\omega L_s)}\right|.\end{aligned} \tag{12}$$

The above equations demonstrate that the mutual inductance between primary and secondary windings plays an important role in the compensation network efficiency. Moreover, to achieve the desired input/output condition, the required operating frequency needs to be tuned. When the LCT is built, the primary and secondary self-inductances are almost fixed. However, the mutual inductance could be significantly affected when gap changes or misalignments occur. Therefore, the compensation network efficiency is closely related to the coupling coefficient *k*, which is calculated as

$$k = \frac{M}{\sqrt{L_p L_s}}. \tag{13}$$

C. Effect of Coupling Coefficient on Compensation Network Efficiency

To study the coupling coefficient variation effect due to gap and misalignment change on the compensation network efficiency, mutual inductance in the efficiency equation is varied while keeping the other parameters constant. The predetermined value of the compensation network parameters is listed in Table III.

Fig. 4 shows the SS compensation network efficiency, phase of impedance, output voltage, and output power as a function of operating frequency with three different coupling coefficients under 20-V dc input condition. The dashed lines indicate that for different coupling coefficient conditions, to achieve same output voltage and output power, the required operating frequency is different. In this example, to obtain 20-V dc output as well as 100-W output power, the operating frequencies from low coupling condition to high coupling condition are 530.8, 559.4, and 591.2 kHz, respectively. The phase of total impedance curve depicts that under 20-V output condition, when the coupling coefficient increases, the phase angle decreases, which means the circulating energy loss is low for high coupling conditions. The efficiency curve also confirms that lower coupling coefficient results in lower efficiency with the same output condition.

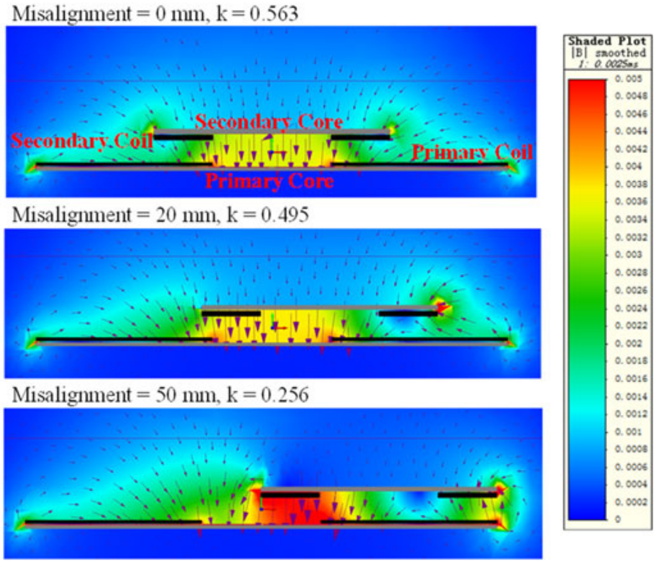

Fig. 10. Magnetic field distribution when $\mathrm{ID}_{\mathrm{Pri}} = 50$ mm, $\mathrm{ID}_{\mathrm{Sec}} = 50$ mm.

Similar results can be drawn from the equations of SP and LLC compensation network cases, which indicate that to achieve same input/output condition, the corresponding operating frequency will increase as the coupling coefficient of the LCT increases, and the compensation network efficiency will increase as well. In order to accommodate different gap variation and misalignment conditions, some design considerations of the LCT are carried out to minimize the coupling coefficient deviation so as to reduce the operating frequency and system efficiency variation.

III. DESIGN CONSIDERATIONS FOR GAP VARIATION AND MISALIGNMENT TOLERANCE

Most LCTs are designed to be symmetrical for transmitter and receiver coil. This configuration could achieve good coupling coefficient when the coils are perfectly aligned under desired gap distance condition. However, when gap variation or misalignment occurs, the coupling coefficient will drop drastically as the simulation results shown in Fig. 5. The primary and

$$\left|\frac{V_{o\_\mathrm{SS}}}{V_{\mathrm{in\_SS}}}\right| = \left|\frac{I_{s\_\mathrm{SS}} R_{o\_\mathrm{ac}}}{I_{p\_\mathrm{SS}} Z_{T\_\mathrm{SS}}}\right| = \left|\frac{j\omega M \cdot R_{o\_\mathrm{ac}}}{\omega^2 M^2 + (r_p + j\omega L_p + 1/j\omega C_p)(r_s + R_{o\_\mathrm{ac}} + j\omega L_s + 1/j\omega C_s)}\right| \tag{5}$$

secondary outer diameter is 100 mm, and inner diameter is 50 mm in the simulation.

Some simulation models are developed in the 3-D FEA simulation tool MagNet to explore the relationships between the LCT coupling coefficient and several key parameters of the coil dimensions. An example model is illustrated in Fig. 6. Fig. 6(a) shows the placement of the LCT with ferrite cores on both sides. The windings and cores are separate from their real position with some gap in order to depict the configuration more clearly. In real design and FEA simulation, the ferrite plates are put close to the coils to help shape the magnetic flux distribution and reduce the radiative interference to the ambient environment. Fig. 6(b) shows the top view of the investigated model excluding the ferrite cores. The simulation parameters are listed in Table IV. As shown in Fig. 6(b), the primary outer diameter $\mathrm{OD}_{\mathrm{pri}}$ and secondary outer diameter $\mathrm{OD}_{\mathrm{sec}}$ are kept to 200 and 100 mm, respectively.

The simulation circuit used in the FEA simulation software is connected as depicted in Fig. 7(a). A current source is directly fed into the primary coil, and the secondary coil is open circuit. In this case, the mutual inductance can be derived as

$$M = \frac{N_s \Phi_{21}}{I_1} \tag{14}$$

where N_s represents the secondary winding turns number, and Φ_{21} is the magnetic flux generated from primary winding and coupled to the secondary winding. Since in the following simulation cases, the winding turns number and injected primary current is maintained the same, *M* is proportional to Φ_{21}, which can be translated to the magnetic flux density *B*. Moreover, when gap variation or misalignment occurs, L_p and L_s are almost constant, which means the coupling coefficient *k* is dependent on the mutual inductance *M*.

From the decoupled model as shown in Fig. 7(b), the relationship between the primary voltage and secondary voltage can be derived as

$$\left|\frac{V_2}{V_1}\right| = \frac{M}{L_p} = k\sqrt{\frac{L_s}{L_p}}. \tag{15}$$

Equation (15) indicates that the voltage gain of the LCT is dependent on the coupling coefficient *k*.

A. Primary Coil Inner Diameter Smaller Than Secondary Coil Outer Diameter

Two scenarios are examined when keeping the primary inner diameter $\mathrm{ID}_{\mathrm{pri}}$ to be 50 mm, while changing the secondary coil inner diameter $\mathrm{ID}_{\mathrm{sec}}$ between 50 and 75 mm. The coupling coefficient *k* when the gap distance varies from 6 to 20 mm under the perfect aligned condition is plotted in Fig. 8(a). The coupling coefficient *k* under the condition of the horizontal misalignment changes from 0 to 50 mm when the air gap is fixed to 10 mm is illustrated in Fig. 8(b). Fig. 8(a) depicts that when the primary winding inner diameter is smaller than the secondary winding outer diameter, the coupling coefficient *k* decreases almost linearly when the gap distance increases, but not much. On the other hand, Fig. 8(b) shows that the coupling coefficient *k* decreases dramatically when the horizontal misalignment becomes larger. Moreover, with larger inner diameter of the secondary winding, the coupling coefficient *k* is slightly larger.

B. Vary Inner Diameter of Primary Coil

Three situations are evaluated when keeping the secondary inner diameter $\mathrm{ID}_{\mathrm{sec}}$ to be 50 mm, while changing the inner diameter of primary coil $\mathrm{ID}_{\mathrm{pri}}$ among 50, 100, and 150 mm. The coupling coefficient when gap distance varies from 6 to 20 mm under perfect aligned condition is plotted in Fig. 9(a), and horizontal misalignment changes from 0 to 50 mm when gap is fixed to 10 mm is illustrated in Fig. 9(b).

Fig. 9 shows that when the primary inner diameter is larger than the secondary outer diameter, coupling coefficient *k* as a function of both gap distance and misalignment looks more like a parabola. The maximum coupling coefficient $k_{\max}$ occurs at a larger gap distance or misalignment when the primary coil inner diameter is larger. Furthermore, coupling coefficient *k* is less sensitive to gap distance and misalignment variation when $\mathrm{ID}_{\mathrm{Pri}} \geq \mathrm{OD}_{\mathrm{Sec}}$. However, it is also obvious that with larger inner diameter of primary winding, coupling coefficient under perfect aligned or small gap condition is smaller.

The magnetic field distributions when $\mathrm{ID}_{\mathrm{Pri}} = 50$ mm and $\mathrm{ID}_{\mathrm{Sec}} = 50$ mm for three different misalignment conditions with 10-mm gap are shown in Fig. 10. The top and bottom gray block represents the cross section of secondary and primary ferrite core, respectively. The primary and secondary windings are illustrated by the dark bars. Different color represents different magnetic intensity as the legend bar shows, from 0 to 5 mT, the color changes from blue to red. The arrows indicate the flux line direction and the arrow size represents the magnetic field strength. Based on (14), the coupling coefficient *k* can be revealed by the magnetic field density *B* near the secondary coil. The top chart and middle chart has similar magnetic field intensity around the secondary coil; hence, the coupling coefficients for these two conditions are similar. The bottom chart demonstrates high *B* near the left edge of secondary coil, but for the rest of the field B fades out. Therefore, the coupling coefficient for the bottom chart is smaller compared with the upper two charts, as the coupling coefficient plot shown in Fig. 9(b).

$$\eta_{T\_\mathrm{SP}} = \frac{R_{o\_\mathrm{ac}}}{R_{o\_\mathrm{ac}} + r_s + \omega^2 C_s^2 R_{o\_\mathrm{ac}}^2 r_s + r_p \frac{(L_s + C_s R_{o\_\mathrm{ac}} r_s)^2}{M^2} + r_p \frac{(r_s + (1 - \omega^2 L_s C_s) R_{o\_\mathrm{ac}})^2}{\omega^2 M^2}} \tag{9}$$

$$\left|\frac{V_{o\_\mathrm{SP}}}{V_{\mathrm{in}\_\mathrm{SP}}}\right| = \left|\frac{j\omega M \cdot R_{o\_\mathrm{ac}}}{\omega^2 M^2 (1 + j\omega C_s R_{o\_\mathrm{ac}}) + [R_{o\_\mathrm{ac}} + (r_s + j\omega L_s)(1 + j\omega C_s R_{o\_\mathrm{ac}})](r_p + j\omega L_p + 1/\omega C_p)}\right| \tag{10}$$

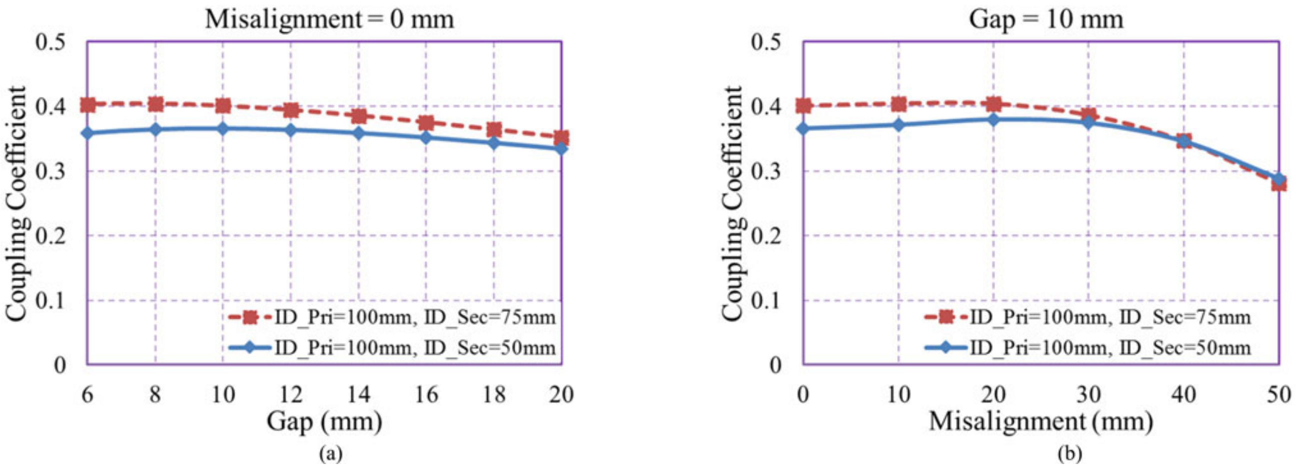

Fig. 11. Coupling coefficient for different secondary coil inner diameter: (a) under gap variation but perfect aligned condition; (b) under misaligned but fixed gap condition.

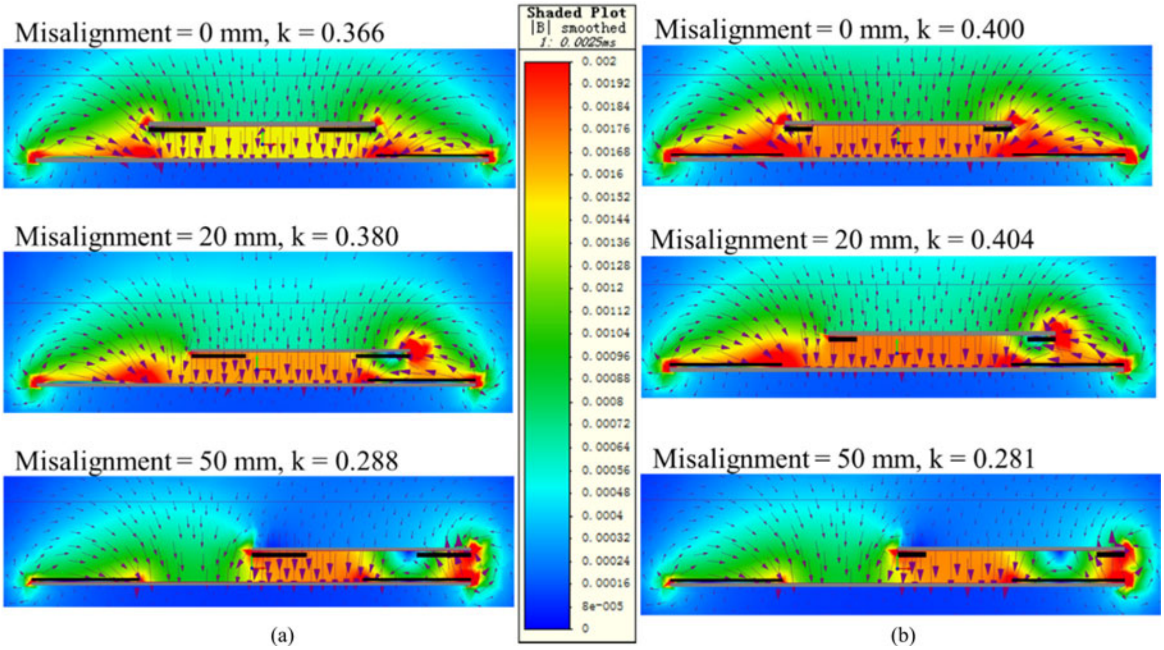

Fig. 12. Magnetic field distribution when (a) $\mathrm{ID_{Pri}} = 100$ mm, $\mathrm{ID_{Sec}} = 50$ mm and (b) $\mathrm{ID_{Pri}} = 100$ mm, $\mathrm{ID_{Sec}} = 75$ mm.

C. Vary Inner Diameter of Secondary Coil

Two examples are checked when keeping the primary inner diameter $\mathrm{ID_{pri}}$ to be 100 mm which equals the secondary coil outer diameter $\mathrm{OD_{sec}}$, while changing the secondary coil inner diameter $\mathrm{ID_{sec}}$ between 50 and 75 mm. The coupling coefficient when gap distance varies from 6 to 20 mm under perfect aligned condition is plotted in Fig. 11(a), and horizontal misalignment changes from 0 to 50 mm when gap is fixed to 10 mm is illustrated in Fig. 11(b).

Fig. 11 indicates that with larger secondary inner diameter, averaged coupling coefficient k is larger. Moreover, with smaller secondary inner diameter, coupling coefficient k is less sensitive to misalignment variation.

The magnetic field distribution for fixed 100-mm inner diameter of primary coil and two different secondary coils with 50- and 75-mm inner diameter under three misalignment conditions are shown in Fig. 12. In both scenarios, the primary coil inner diameter equals the secondary coil outer diameter, and the gap is fixed at 10 mm. For either $\mathrm{ID_{Sec}}$ case under 0- and 20-mm misalignment conditions, the magnetic intensity around the secondary coil are similar; hence, the coupling coefficients variations are minor. When the misalignment increases to 50 mm, the induced magnetic field coupled to the secondary coil drops; therefore, the coupling coefficient decreases. From the comparison between Fig. 12(a) and (b), the averaged magnetic field intensity is higher for the secondary coil with larger inner diameter when misalignment is 0 and 20 mm, which results in higher coupling coefficient as shown in Fig. 11(b). For 50-mm misalignment condition, both cases demonstrates similar magnetic field distribution, which lead to almost equal coupling coefficient as depicted in Fig. 11(b).

IV. EXPERIMENTAL VERIFICATION

To verify the efficiency analysis and design considerations based on the FEA simulation results, a 100-W lab prototype is built as shown in Fig. 13(a), and the circuit diagram is depicted in Fig. 13(b). The input dc voltage is set at 20 V, and the output dc voltage is regulated at 20 V; hence, the full load output current is 5 A. The switching devices Q_1-Q_4 used for the primary high-frequency inverter are the OptiMOS BSC052N03LS from Infineon, and the secondary rectifier bridge D_1-D_4 uses Schottky diode PDS1040 L from Diodes Inc. Three 5PT46N103 capacitors from Electronic Concepts are series together to form a 3.33-nF resonant capacitor C_p. Two LCTs are implemented to compare the coupling coefficient and compensation network efficiency when gap variation or misalignment occurs. Both the LCT primary and secondary are made of NELD1050/44SNSN from New England, which is equivalent 14 AWG litz wire consisting of 1050 strands of 44 AWG wire. The 4:4 symmetrical LCT consists of primary and secondary coils both with inner diameter 77 mm and outer diameter 95 mm. Both primary and secondary winding resistances r_p and r_s for the symmetrical LCT are around 35 mΩ. The 10:4 asymmetrical LCT comprises a transmitter coil with 153-mm outer diameter and 110-mm inner diameter, and a receiver coil with 95-mm outer diameter and 77-mm inner diameter. The transmitter and receiver winding resistance are 135 and 35 mΩ, respectively. Twelve pieces of ferrite bars with material 3C94 are placed beneath the primary coil to help shape the magnetic flux distribution and decrease radiated interference to ambient environment. GW Instek LCR-821 digital LCR meter which has a precision of 0.05% is used to measure the self and mutual inductances in order to calculate the coupling coefficient.

Fig. 14 shows the comparison between the measured and FEA simulated coupling coefficient for different gap distance and misalignment conditions for the symmetrical LCT. The experimental results agree well with the simulated results. When the primary and secondary windings are perfectly aligned, and the gap distance changes from 6 to 20 mm, the coupling coefficient drops from 0.441 to 0.141, which represents 68% reduction. When the gap is fixed at 10 mm, and the misalignment changes from 0 to 50 mm, the coupling coefficient drops from 0.354 to 0.038, or 89% reduction.

Fig. 15 illustrates the comparison between the measured and FEA simulated coupling coefficient for different gap distance and misalignment conditions for the asymmetrical LCT. When the primary and secondary coils are perfectly aligned, and the gap distance changes from 6 to 20 mm, the coupling coefficient ranges from 0.3 to 0.216, or 28% reduction. When the gap is fixed at 10 mm, and the misalignment changes from 0 to 50 mm, the coupling coefficient ranges from 0.312 to 0.215, or 31% reduction. The coupling coefficient deviation for the designed asymmetrical LCT is much smaller compared to that of the symmetrical LCT.

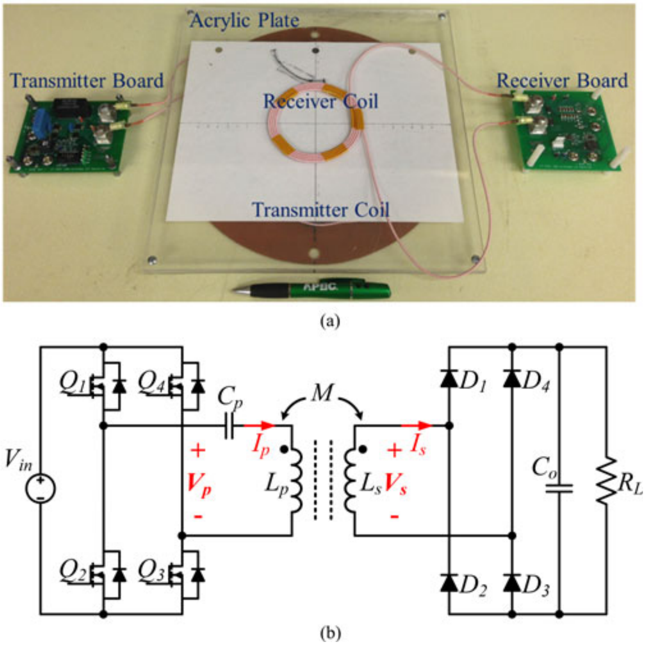

Fig. 13. IPT system (a) experimental prototype and (b) circuit diagram.

Fig. 16 compares the main operation waveforms of the IPT system under full-load condition for the symmetrical LCT with 10-mm gap under different misalignment conditions. The operating frequencies for 0- and 40-mm misalignment conditions are 520 and 432 kHz, respectively. Under perfectly aligned condition, the phase angle between the high-frequency inverter output voltage and current is small; hence, the circulating energy loss is small. When misalignment increases to 40 mm, the phase angle increases, so does the primary current, which compromises the compensation network efficiency but maintains full power transfer. These results agree with the analysis discussed in Section II which indicates that to achieve same input/output condition, the corresponding operating frequency will increase as the coupling coefficient of the LCT increases, and the compensation network efficiency will increase as well.

Fig. 17 compares the full-load efficiency between the symmetrical and the asymmetrical LCT under different gap distance and misalignment conditions. When the transmitter and receiver coils are in perfect aligned position and the gap distance changes from 6 to 20 mm, the system efficiency for the symmetrical and the asymmetrical LCT ranges from 88.56% to 76.99% and 86.48% to 82.98%, respectively. When the gap is fixed at 10 mm, and the misalignment increases from 0 to 50 mm, the system efficiency for the symmetrical LCT drops from 87.5% to 59.6% due to a large primary side current. With the asymmetrical LCT, however, the system efficiency stays around 86% when the misalignment is less than 40 mm. The efficiency results verify the analysis in previous section, which indicates that higher coupling coefficient results in higher compensation

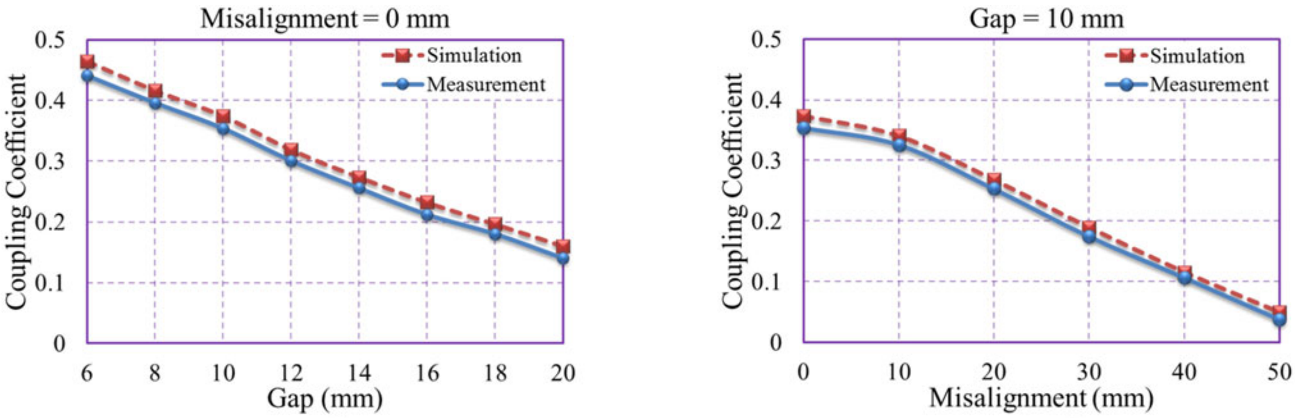

(a) (b)

Fig. 14. Coupling coefficient for the symmetrical LCT: (a) under gap variation but perfect aligned condition; (b) under misaligned but fixed gap condition.

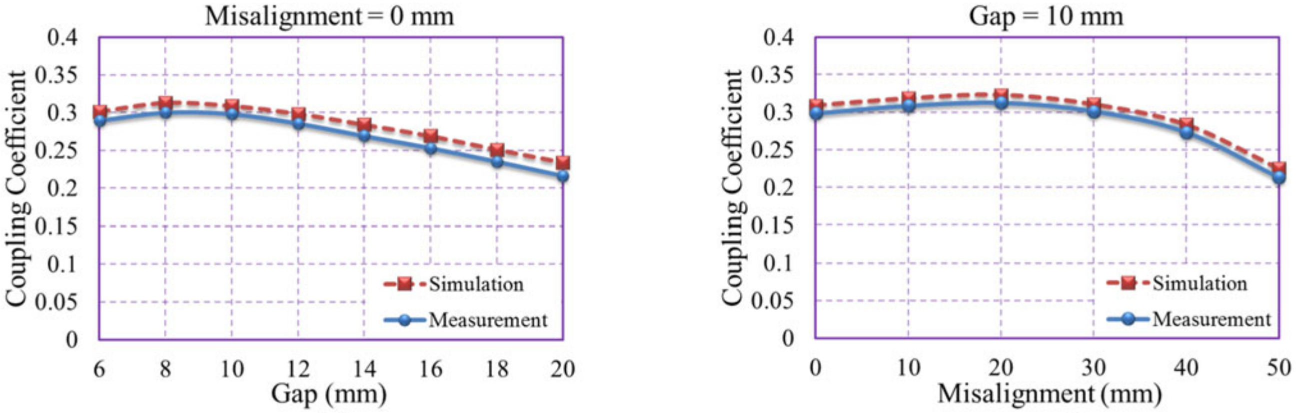

(a) (b)

Fig. 15. Coupling coefficient for the asymmetrical LCT: (a) under gap variation but perfect aligned condition; (b) under misaligned but fixed gap condition.

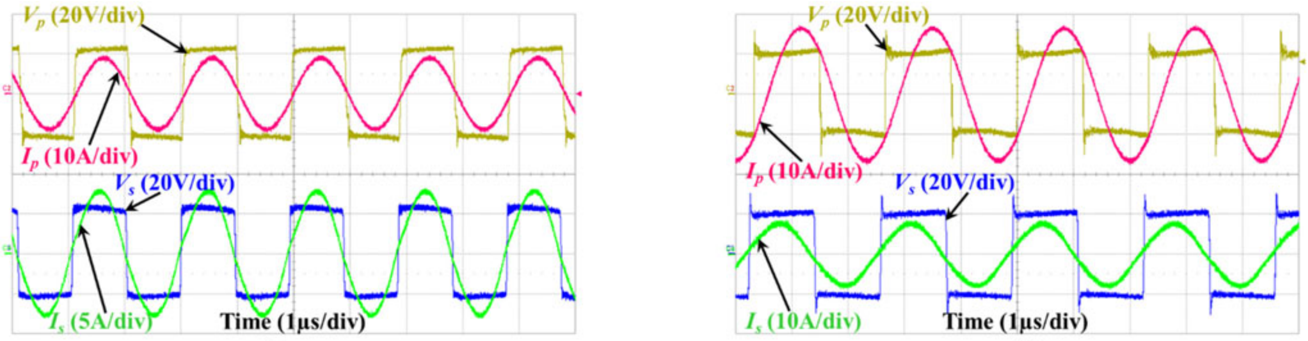

(a) (b)

Fig. 16. Main waveforms under full-load condition for the symmetrical LCT with 10-mm gap and (a) 0-mm misalignment and (b) 40-mm misalignment.

network efficiency. Moreover, with the proposed asymmetrical LCT design, the coupling coefficient varies slightly over the entire misalignment range, and thus, the efficiency curve maintains nearly flat. For real implementation, the system efficiency will suffer when put under the ferrous chassis of the laptop or EV, especially for low coupling conditions. These effects can be mostly mitigated by adding some ferrite sheet on the top of the receiver pad for the shielding purpose.

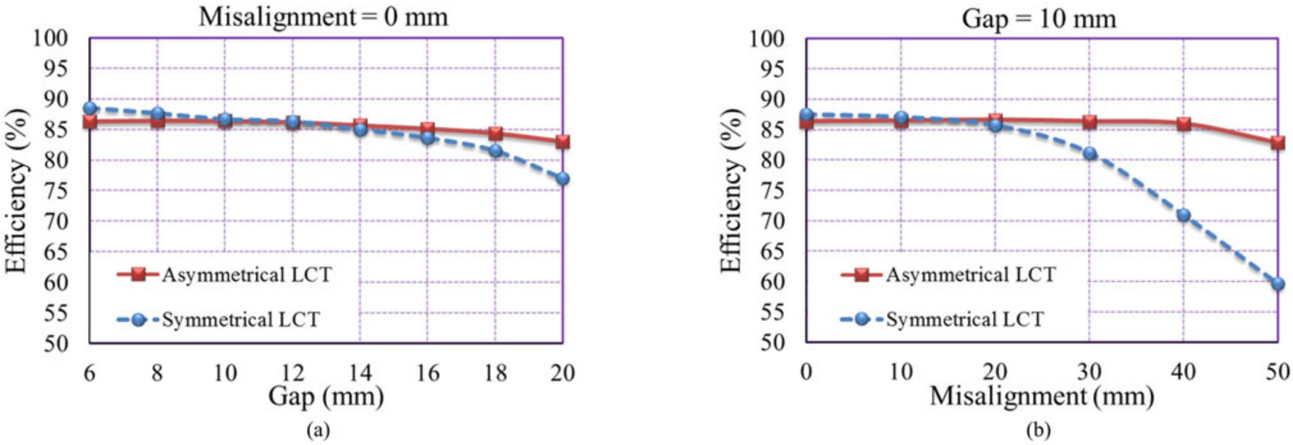

Fig. 17. Efficiency comparison between the symmetrical LCT and the asymmetrical LCT: (a) under gap variation but perfect aligned condition; (b) under misaligned but fixed gap condition.

V. CONCLUSION

This paper discusses some design considerations to reduce gap variation and misalignment effects for the IPT system. The significance of coupling coefficient of the LCT to the compensation network efficiency is carefully analyzed. With the aid of FEA simulation software, the flux distribution and coupling coefficient of the transmitter and receiver coil with different dimension parameters can be compared. Through the FEA simulation results and the corresponding analysis, key design considerations can be drawn as follows.

1) An LCT with larger inner diameter primary coil tends to have a less sensitive coupling coefficient when gap distance and misalignment change. However, the averaged coupling coefficient is lower for this case.
2) When the inner diameter of secondary winding increases, the averaged coupling coefficient will increase, but it is more sensitive to gap and misalignment variations.

In order to validate the performance of the proposed design considerations, a 100-W hardware prototype with a symmetrical LCT and the proposed asymmetrical LCT has been built and tested. The experimental results demonstrate that the designed asymmetrical LCT prototype maintains the coupling coefficient in a relatively flat region. For example, under fully aligned condition, the coupling coefficient varies from 0.3 to 0.216 when the gap increases from 6 to 20 mm. For the test condition with 10-mm gap condition, the coupling coefficient varies from 0.312 to 0.215 when the misalignment varies from 0 to 50 mm. For comparison purpose, the symmetrical LCT case would have coupling coefficient varying from 0.354 to 0.038.

With a relatively flat coupling coefficient under gap variation and misalignment conditions, the system efficiency maintains nearly flat over the entire test range. The maximum efficiency deviation with the asymmetrical LCT is kept within 3.5% over the entire 50-mm misalignment range. Again, for comparison purpose, the system efficiency with the symmetrical LCT deviates 27.9% over the 50-mm misalignment range. Overall, the proposed asymmetrical LCT design methodology demonstrates an effective way of dealing with a wide range of gap variation and misalignment for IPTs.

REFERENCES

[1] C. Wang, O. H. Stielau, and G. A. Covic, “Design considerations for a contactless electric vehicle battery charger,” *IEEE Trans. Ind. Electron.*, vol. 52, no. 5, pp. 1308–1314, Oct. 2005.

[2] J. Sallan, J. Villa, A. Llombart, and J. Sanz, “Optimal design of ICPT systems applied to electric vehicle battery charge,” *IEEE Trans. Ind. Electron.*, vol. 56, no. 6, pp. 2140–2149, Jun. 2009.

[3] H. H. Wu, A. Gilchrist, K. D. Sealy, and D. Bronson, “A high efficiency 5 kW inductive charger for EVs using dual side control,” *IEEE Trans. Ind. Informat.*, vol. 8, no. 3, pp. 585–595, Aug. 2012.

[4] G. A. Covic and J. T. Boys, “Modern trends in inductive power transfer for transportation applications,” *IEEE J. Emerg. Sel. Topics Power Electron.*, vol. 1, no. 1, pp. 28–41, Mar. 2013.

[5] S. M. Lukic, “Cutting the cord, static and dynamic inductive wireless charging of electric vehicles,” *IEEE Electrification Mag.*, vol. 1, no. 1, pp. 57–65, Sep. 2013.

[6] S. Lee, B. Choi, and C. T. Rim, “Dynamics characterization of the inductive power transfer system for online electric vehicles by Laplace phasor transform,” *IEEE Trans. Power Electron.*, vol. 28, no. 12, pp. 5902–5909, Dec. 2013.

[7] S. Y. Choi, B. W. Gu, S. W. Lee, W. Y. Lee, J. Huh, and C. T. Rim, “Generalized active EMF cancel methods for wireless electric vehicles,” *IEEE Trans. Power Electron.*, vol. 29, no. 11, pp. 5770–5783, Nov. 2014.

[8] C. Zheng, J.-S. Lai, R. Chen, W. E. Faraci, Z. U. Zahid, B. Gu, L. Zhang, G. Lisi, and D. Anderson, “High-efficiency contactless power transfer system for electric vehicle battery charging application,” *IEEE J. Emerg. Sel. Topics Power Electron.*, vol. 3, no. 1, pp. 65–74, Mar. 2015.

[9] K. Chang-Gyun, S. Dong-Hyun, Y. Jung-Sik, P. Jong-Hu, and B. H. Cho, “Design of a contactless battery charger for cellular phone,” *IEEE Trans. Ind. Electron.*, vol. 48, no. 6, pp. 1238–1247, Dec. 2001.

[10] S. Y. R. Hui and W. W. C. Ho, “A new generation of universal contactless battery charging platform for portable consumer electronic equipment,” *IEEE Trans. Power Electron.*, vol. 20, no. 3, pp. 620–627, May 2005.

[11] C.-H. Hu, C.-M. Chen, Y.-S. Shiao, T.-J. Chan, and T.-R. Chen, “Development of a universal contactless charger for handheld devices,” in *Proc. IEEE Int. Symp. Ind. Electron.*, 2008, pp. 99–104.

[12] S. Y. Hui, “Planar wireless charging technology for portable electronic products and Qi,” *Proc. IEEE*, vol. 101, no. 6, pp. 1290–1301, Jun. 2013.

[13] F. Sato, T. Nomoto, G. Kano, H. Matsuki, and T. Sato, “A new contactless power signal transmission device for implanted functional electrical stimulation (FES),” *IEEE Trans. Magn.*, vol. 40, no. 4, pp. 2964–2966, Apr. 2004.

[14] G. Wang, W. Liu, M. Sivaprakasam, and G. A. Kendir, “Design and analysis of an adaptive transcutaneous power telemetry for biomedical implants,” *IEEE Trans. Circuits Syst. I, Reg. Papers*, vol. 52, no. 10, pp. 2109–2117, Oct. 2005.

[15] H. Miura, S. Arai, Y. Kakubari, F. Sato, H. Matsuki, and T. Sato, “Improvement of the transcutaneous energy transmission system utilizing ferrite cored coils for artificial hearts,” *IEEE Trans. Magn.*, vol. 42, no. 10, pp. 3578–3580, Oct. 2006.

[16] K. Chen, Z. Yang, L. Hoang, J. Weiland, M. Humayun, and W. Liu, "An integrated 256-channel epiretinal prosthesis," *IEEE J. Solid-State Circuits*, vol. 45, no. 9, pp. 1946–1956, Sep. 2010.

[17] A. Ram Rakhyani, S. Mirabbasi, and M. Chiao, "Design and optimization of resonance-based efficient wireless power delivery systems for biomedical implants," *IEEE Trans. Biomed. Circuits Syst.*, vol. 5, no. 1, pp. 48–63, Feb. 2011.

[18] H. Cao, V. Landge, U. Tata, Y. Seo, S. Rao, S. J. Tang, H. F. Tibbals, S. J. Spechler, and J.-C. Chiao, "An implantable, batteryless, and wireless capsule with integrated impedance and pH sensors for gastroesophageal reflux monitoring," *IEEE Trans. Biomed. Eng.*, vol. 59, no. 11, pp. 3131–3199, Nov. 2012.

[19] W. M. Ng, C. Zhang, D. Lin, and S. Y. Ron Hui, "Two- and three-dimensional omnidirectional wireless power transfer," *IEEE Trans. Power Electron.*, vol. 29, no. 9, pp. 4475–4478, Sep. 2014.

[20] R. Wu, W. Li, H. Luo, J. K. O. Sin, and C. C. Yue, "Design and characterization of wireless power links for brain-machine interface applications," *IEEE Trans. Power Electron.*, vol. 29, no. 10, pp. 5462–5471, Oct. 2014.

[21] W. Zhong, X. Liu, and S. Y. R. Hui, "A novel single-layer winding array and receiver coil structure for contactless battery charging systems with free-positioning and localized charging features," *IEEE Trans. Ind. Electron.*, vol. 58, no. 9, pp. 4136–4144, Sep. 2011.

[22] A. K. RamRakhyani and G. Lazzi, "Multicoil telemetry system for compensation of coil misalignment effects in implantable systems," *IEEE Antennas Wireless Propag. Lett.*, vol. 11, pp. 1675–1678, 2012.

[23] K. Mori, L. Hyunkeun, S. Iguchi, K. Ishida, M. Takamiya, and T. Sakurai, "Positioning-free resonant wireless power transmission sheet with staggered repeater coil array (SRCA)," *IEEE Antennas Wireless Propag. Lett.*, vol. 11, pp. 1710–1713, 2012.

[24] J. P. C. Smeets, T. T. Overboom, J. W. Jansen, and E. A. Lomonova, "Comparison of position-independent contactless energy transfer systems," *IEEE Trans. Power Electron.*, vol. 28, no. 4, pp. 2059–2067, Apr. 2013.

[25] H. R. Ahn, M. S. Kim, and Y. J. Kim, "Inductor array for minimising transfer efficiency decrease of wireless power transmission components at misalignment," *Electron. Lett.*, vol. 50, no. 5, pp. 393–394, Feb. 2014.

[26] M. L. G. Kissin, C. Y. Huang, G. A. Covic, and J. T. Boys, "Detection of the tuned point of a fixed-frequency *LCL* resonant power supply," *IEEE Trans. Power Electron.*, vol. 24, no. 4, pp. 1140–1143, Apr. 2009.

[27] H. Wu, G. Covic, J. Boys, and D. Robertson, "A series-tuned inductive-power-transfer pickup with a controllable AC-voltage output," *IEEE Trans. Power Electron.*, vol. 26, no. 1, pp. 98–109, Jan. 2011.

[28] J. L. Villa, J. Sallan, J. F. Sanz Osorio, and A. Llombart, "High-misalignment tolerant compensation topology for ICPT systems," *IEEE Trans. Ind. Electron.*, vol. 59, no. 2, pp. 945–951, Feb. 2012.

[29] M. Pinuela, D. C. Yates, S. Lucyszyn, and P. D. Mitcheson, "Maximizing DC-to-load efficiency for inductive power transfer," *IEEE Trans. Power Electron.*, vol. 28, no. 5, pp. 2437–2447, May 2013.

[30] S. Aldhaher, P. C.-K. Luk, and J. F. Whidborne, "Tuning class E inverters applied in inductive links using saturable reactors," *IEEE Trans. Power Electron.*, vol. 29, no. 6, pp. 2969–2978, Jun. 2014.

[31] Y. Lim, H. Tang, S. Lim, and J. Park, "An adaptive impedance-matching network based on a novel capacitor matrix for wireless power transfer," *IEEE Trans. Power Electron.*, vol. 29, no. 8, pp. 4403–4413, Aug. 2014.

[32] S. Aldhaher, P. C.-K. Luk, and J. F. Whidborne, "Electronic tuning of misaligned coils in wireless power transfer systems," *IEEE Trans. Power Electron.*, vol. 29, no. 11, pp. 5975–5982, Nov. 2014.

[33] K. Fotopoulou and B. W. Flynn, "Wireless power transfer in loosely coupled links: Coil misalignment model," *IEEE Trans. Magn.*, vol. 47, no. 2, pp. 416–430, Feb. 2011.

[34] J. Acero, C. Carretero, I. Lope, R. Alonso, O. Lucia, and J. M. Burdio, "Analysis of the mutual inductance of planar-lumped inductive power transfer systems," *IEEE Trans. Ind. Electron.*, vol. 60, no. 1, pp. 410–420, Jan. 2013.

[35] B. W. Flynn and K. Fotopoulou, "Rectifying loose coils: Wireless power transfer in loosely coupled inductive links with lateral and angular misalignment," *IEEE Microw. Mag.*, vol. 14, no. 2, pp. 48–54, Mar./Apr. 2013.

[36] S. Raju, R. Wu, M. Chan, and C. P. Yue, "Modeling of mutual coupling between planar inductors in wireless power applications," *IEEE Trans. Power Electron.*, vol. 29, no. 1, pp. 481–490, Jan. 2014.

[37] M. Q. Nguyen, Z. Hughes, P. Woods, Y.-S. Seo, S. Rao, and J.-C. Chiao, "Field distribution models of spiral coil for misalignment analysis in wireless power transfer systems," *IEEE Trans. Microw. Theory Tech.*, vol. 62, no. 4, pp. 920–930, Apr. 2014.

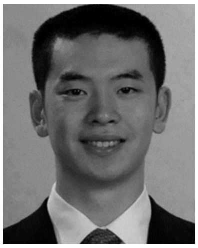

Cong Zheng (S'11) received the B.S. degree from Tsinghua University, Beijing, China, and the M.S. degree from the Illinois Institute of Technology, Chicago, IL, USA, in 2005 and 2009, respectively, both in electrical engineering. He is currently working toward the Ph.D. degree in electrical engineering from the Virginia Polytechnic Institute and State University, Blacksburg, VA, USA.

Since 2009, he has been a Graduate Research Assistant with the Future Energy Electronics Center, Virginia Tech. His current research interests include contactless power transfer, LED driving circuits, energy harvesting, and renewable energy applications.

Hongbo Ma (S'11–M'12) received the B.S. degree from Lanzhou Jiaotong University, Lanzhou, China, and the Ph.D. degree from the Southwest Jiaotong University, Chengdu, China, in 2004 and 2012, respectively, both in electrical engineering.

From September 2009 to October 2011, he was a Research Assistant at the Future Energy Electronics Center, Virginia Polytechnic Institute and State University, Blacksburg, VA, USA. From December 2012 to July 2013, he was a Postdoctoral Research Fellow at National Taiwan University of Science and Technology (NTUST), Taiwan. In November 2012, he joined the School of Electrical Engineering, Southwest Jiaotong University, where he is currently an assistant professor and advisor for master student supported by the introduced talents plan. Meanwhile, he is also a research fellow in the NTUST Power Electronics Center. He is the author or coauthor of more than 50 technical papers published in journals and conference. His main research interests include high efficiency power converters for rail-way traffic applications, LED Lighting drivers, and renewable energy power conditioning systems.

Jih-Sheng Lai (S'85–M'89–SM'93–F'07) received the M.S. and Ph.D. degrees in electrical engineering from the University of Tennessee, Knoxville, TN, USA, in 1985 and 1989, respectively.

In 1989, he joined the Electric Power Research Institute (EPRI) Power Electronics Applications Center, where he managed EPRI-sponsored power electronics research projects. In 1993, he then joined the Oak Ridge National Laboratory as the Power Electronics Lead Scientist, where he initiated a high power electronics program and developed several novel high-power converters including multilevel converters and soft-switching inverters. In 1996, he joined the Virginia Polytechnic Institute and State University, where he is currently the James S. Tucker Professor at Electrical and Computer Engineering Department and the Director of Future Energy Electronics Center. He has published more than 295 technical papers and two books and received 22 U.S. patents. His current research interests include high-efficiency power electronics conversions for high power and energy applications.

Dr. Lai is the recipient of several distinctive awards including a Technical Achievement Award in Lockheed Martin Award Night, three IEEE IAS Conference Paper Awards, and Best Paper Awards from IECON-97, IPEC-05, and PCC-07. His student teams won the first place award from 2009 TI Enginous Prize Analog Design Competition and 2011 Grand Prize Award from International Future Energy Challenge. He chaired the 2000 IEEE Workshop on Computers in Power Electronics, 2001 IEEE/DOE Future Energy Challenge, and 2005 IEEE Applied Power Electronics Conference and Exposition.

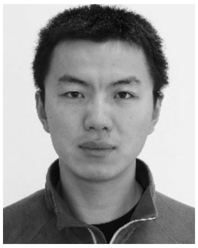

Lanhua Zhang (S'13) received the B.S. and M.S. degrees in electrical engineering from Shandong University, Shandong, China, in 2009 and 2012, respectively. He is currently working toward the Ph.D. degree at the Future Energy Electronics Center, Virginia Tech, Blacksburg, VA, USA.

Since 2012, he has been a Graduate Research Assistant at Future Energy Electronics Center, Virginia Tech, Blacksburg, VA, USA. His research interests include soft-switching inverter for renewable energy application, high-efficiency dc/dc converter, and nonlinear current control technology.